

Origin of Polytype Formation in VLS-Grown Ge Nanowires through Defect Generation and Nanowire Kinking

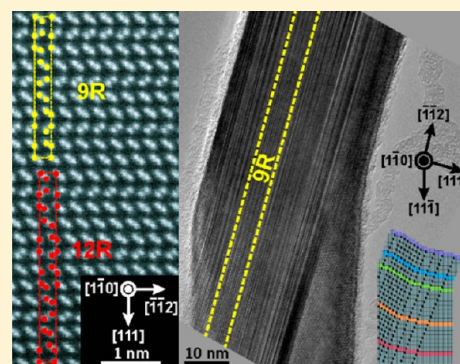
Nari Jeon,[†] Shadi A. Dayeh,[‡] and Lincoln J. Lauhon^{*,†}

[†]Department of Materials Science and Engineering, Northwestern University, Evanston, Illinois 60208, United States

[‡]Department of Electrical and Computer Engineering, University of California—San Diego, La Jolla, California 92093, United States

S Supporting Information

ABSTRACT: We propose layer-by-layer growth mechanisms to account for planar defect generation leading to kinked polytype nanowires. C_s -corrected scanning transmission electron microscopy enabled identification of stacking sequences of distinct polytype bands found in kinked nanowires, and Raman spectroscopy was used to distinguish polytype nanowires from twinned nanowires containing only the 3C diamond cubic phase. The faceting and atomic-scale defect structures of twinned 3C are compared with those of polytype nanowires to develop a common model linking nucleation pinning to nanowire morphology and phase.



KEYWORDS: Nanowire, polytype, VLS growth, TEM, defects, kinking

Among various parameters characterizing a nanowire including size, shape, and composition, the polytype has emerged as an important aspect of investigation.^{1–3} Polytypes open up the possibility to engineer electronic band structure in homojunctions, promising a widened range of electronic and optoelectronic properties.^{4–6} For instance, the reduction in momentum transfer associated with band structure modification was demonstrated in macroporous polytype Si, which can be beneficial in Si-based photovoltaic and light-emitting devices.⁷ III–V polytype nanowires can have regularly spaced twin planes perpendicular to the nanowire axis, exhibiting so-called twinning superlattice structure;^{1,2} defects parallel to the axis of III–V nanowires appear to be nonperiodic.⁸ In contrast, group IV polytype nanowires have exhibited polytype inclusions composed of ordered (111) intrinsic stacking faults parallel to the nanowire axis,^{9–13} though recently planar defects perpendicular to the Si nanowire axis have also been observed.¹⁴ A framework to identify various polytypes in Si nanowires was developed by correlating Raman spectroscopy and transmission electron microscopy (TEM).¹¹ Some of these defect structures parallel to the growth axis may be misinterpreted as polytypes solely from the diffraction patterns and high-resolution TEM images.^{9,15,16} To distinguish polytypes from other possible structures, Raman spectroscopy can be readily exploited.^{9,11} A polytype inclusion in nanowires can also be observed directly by imaging the cross section of nanowire in TEM along certain zone axes.⁹

Lopez et al. reported kinked Si nanowires in which a polytype inclusion is present after the kink.¹¹ This suggests that polytypes need not be seeded from the substrate but that their

formation might be related to nanowire kinking. The growth of kinked nanowires has been realized via changes of pressure that causes change in supersaturation in the vapor–liquid–solid growth.^{17–19} Considering a polytype as an ordered array of planar defects, one should therefore account for formation of planar defects concomitant with nanowire kinking to understand the origin of polytype generation. The formation of planar defects on (111) planes perpendicular to the nanowire growth axis is related with supersaturation of the growth seed in III–V nanowires.²⁰ In group IV nanowires, planar defects on (111) extending along the nanowire axis were observed with a $\langle 112 \rangle$ growth direction.^{12,21} In addition, a coherent $\Sigma 3$ (111) twin boundary was found to induce the growth direction change from $\langle 111 \rangle$ to $\langle 112 \rangle$.²² These prior results lead to the association of polytype formation with variations in supersaturation that induce planar defect formation and nanowire kinking, but it is unclear how step nucleation and propagation on growth fronts lead to ordering in planar defects and the change in growth direction simultaneously.

Here we propose a polytype generation mechanism based on structural analyses of kink-inducing stacking faults in polytype and bicrystalline nanowires. C_s -corrected scanning TEM (STEM) imaging is used to identify the stacking sequence of (111) close-packed planes in different polytype bands. Atomic-scale structures of polytype nanowires are compared with those of twinned bicrystalline nanowires, and layer-by-layer growth mechanisms are described in terms of nucleation site pinning/

Received: June 11, 2013

Published: July 30, 2013

unpinning and evolution of new growth fronts. We utilize this comprehensive analysis to suggest that a growth pseudofacet corresponding to the polytype band evolves on the L–S interface, leading to lateral expansion of the polytype band and eventual nanowire kinking, explaining the evolution of the nanowire morphology.

Ge nanowires were grown by chemical vapor deposition using the vapor–liquid–solid (VLS) process. Au nanoparticles of 20–50 nm diameter were deposited from colloidal solutions onto Si (100) substrates coated with poly(L-lysine). Germane gas (GeH_4) was introduced at the growth temperature of 320 °C with (or without) phosphine gas (PH_3) for n-type (or intrinsic) Ge nanowires. A flow of hydrogen (H_2) gas was maintained during heating and nanowire-growing steps. At the growth temperature, the flow rates of gases were constant ($\text{GeH}_4 = 50$ sccm and $\text{H}_2 = 50$ sccm), but the pressure was modulated to induce kinking and polytype formation. Specifically, the pressure was 150 Torr for 10 min, ~ 0.5 Torr for 20 s, and 500 Torr for the remainder of the growth (5 min). Nanowires were transferred to copper TEM grids coated with lacey carbon films for Raman spectroscopy and TEM imaging. Raman spectra were acquired using a confocal Raman microscope (Witec Alpha300) and analyzed as described in a previous study.¹¹ Low laser powers (10 μW) and signal averaging (30 s per spectrum) were used to minimize laser-induced heating. High-resolution lattice images and diffraction patterns were recorded by a JEOL JEM-2100F at 200 kV. C_s -corrected HRTEM and STEM imaging was conducted using a JEOL JEM-ARM200F at 200 kV.

We first identify the polytypes present in $\langle 112 \rangle$ oriented nanowire segments before considering their origin in kinking from a $\langle 111 \rangle$ growth direction. Figure 1a shows a horizontally oriented nanowire, with a $[\bar{1}\bar{1}2]$ growth direction, exhibiting multiple planar defects on (111) planes parallel to the nanowire growth axis. The outermost portions of the nanowire, at the top and bottom of Figure 1a, have a 3C diamond cubic structure. These two “side bands” are in a twin relationship, indicating that there is an odd number of twin boundaries (at least one) in the nanowire. In between the 3C side bands, there is a high density of planar defects, producing streaks in the (111) reflections in the diffractogram (inset of Figure 1a). Periodic contrast in some regions of the HRTEM image and forbidden reflections between the (111) reflections indicate that the planar defects are periodic in some regions. To identify the polytypes, C_s -corrected high-angle annular dark-field (HAADF) scanning transmission electron microscopy (STEM) imaging was carried out on the same nanowire (Figure 1b). The atomic columns associated with Ge (111) bilayers are well resolved, enabling the identification of three distinct bands in which the intrinsic stacking faults are ordered in 5H, 9R, and 12R polytypes. Figure 1c shows clearly the stacking sequence associated with 9R and 12R polytypes, and Table 1 summarizes common notation schemes.^{23–25} The Ramsdell notation has the merit of simplicity, whereas the Hagg notation explicitly reveals the ABC stacking sequence. The h–k notation is useful in that it directly gives the hexagonality of polytype, i.e., the fraction of hexagonal packing in a unit cell.

Raman spectroscopy confirms the presence of polytypes: the spectrum exhibits two peaks at ~ 298 and ~ 287 cm^{-1} (Figure 1e), whereas a pure 3C nanowire has only one peak ~ 300 cm^{-1} in this region of the spectrum. The single peak in the pure 3C nanowire is a triply degenerate F_{2g} mode of a diamond cubic structure. The high wavenumber peak in the polytype nanowire

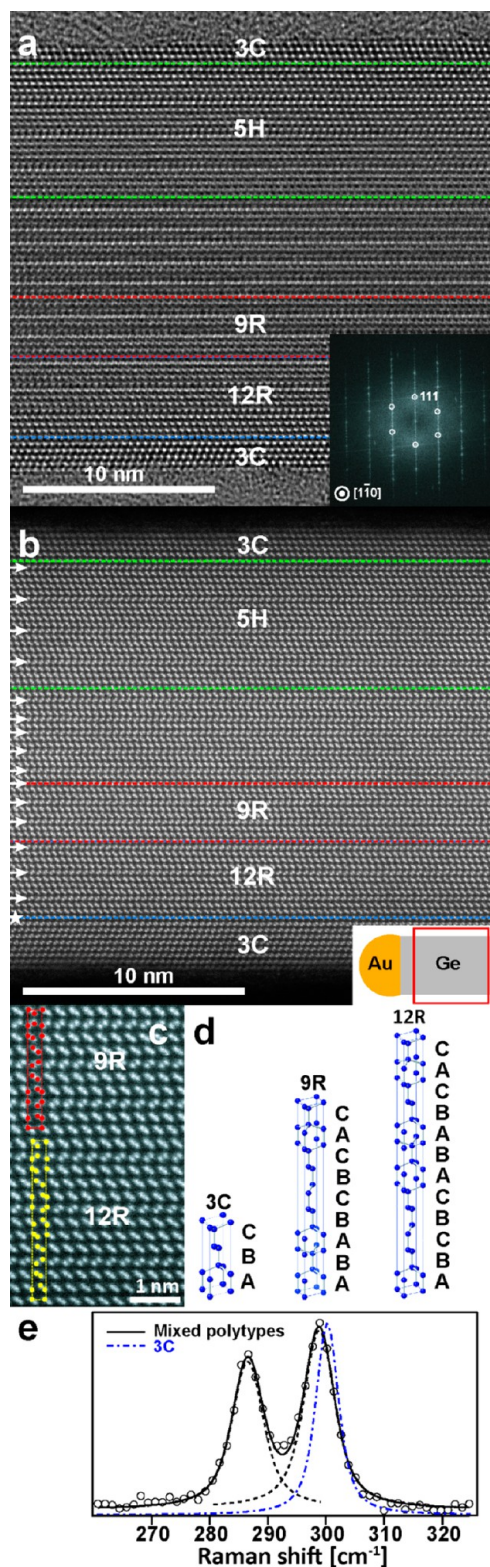


Figure 1. C_s -corrected HRTEM (a) and HAADF-STEM (b) images of a nanowire composed of different polytype bands marked by color dashed lines. The inset of (a) is a diffractogram where white circles indicate reflections of 3C crystals. The inset of (b) is a schematic of nanowire, showing the imaged area in (a) and (b) (a red box). The white arrow and star in (b) indicate the locations of the intrinsic stacking fault and twin boundary, respectively. (c) High-magnification HAADF-STEM image of 9R and 12R band with Ge atomic columns marked in each unit cell. (d) Reconstruction of crystal structures of

Figure 1. continued

3C, 9R, and 12R polytypes in a hexagonal unit cell. Stacking orders of Ge bilayers along the c -axis (ABC) are denoted. (e) Comparison of Raman spectra between the polytype nanowire shown in (a)–(c) and the nanowire of pure 3C phase. Circles are the measured Raman data, and black solid line is the fitted curve with individual peaks (dashed lines) for the polytype nanowire. A blue dash-dotted line is the Raman spectrum of the pure 3C nanowire.

($\sim 298\text{ cm}^{-1}$) is $\sim 2\text{ cm}^{-1}$ lower than that of the 3C nanowire. We assign the high-frequency peak to the axial mode that involves atomic vibrations normal to the faulted (111) planes. In polytypes, the deviation from the stacking sequence of 3C modifies the Raman polarizability tensors, and new peaks arise that are associated with modified Brillouin zone boundaries.^{26,27} The low-frequency peak in the polytype nanowire ($\sim 287\text{ cm}^{-1}$) arises from vibrations within the close-packed plane (i.e., the parallel mode) and is influenced by variations in the short-range order within different polytype bands. This peak, however, is not resolved into distinct modes for each of the polytypes due to the narrow widths of the bands and the limitations of the instrument. We note that a crystal of mixed polytypes with small domains exhibits a Raman peak that can be related to the average stacking sequence.²⁷ Furthermore, a crystal of random stacking sequence also displays a Raman peak in between the Brillouin zone boundaries because it can be viewed as containing multiple domains with distinct short-range ordering in the stacking sequence.^{11,28}

Polytype regions are often found between the nanowire tip (identified by the presence of the growth seed) and a kink from a $\langle 111 \rangle$ type growth direction, as observed earlier for silicon nanowires.¹¹ Recent studies have associated such kinking with the introduction of planar defects²² due to changes in the catalyst supersaturation and/or modification of the energetics at the triple phase boundary. To explore further the connection between kinking and defect generation in the context of the more appealing polytype nanowires and to uncover the mechanism that governs their precisely ordered growth, the pressure was modulated during growth^{17–19} as described above, which increased the yield of kinked nanowires with polytypes. Figure 2 shows a nanowire kinking from a $[111]$ to $[112]$ growth direction, with planar defects and polytype bands originating in the $[111]$ -oriented segment and propagating into the $[112]$ -oriented segment. The defects originate at the outer surface (Figure 2c), where “outer” refers to the surface that the nanowire kinks away from when viewing on a $\langle 110 \rangle$ zone. The 9R polytype inclusions, the planar defect bands, and the 3C bands persist to the nanowire tip; i.e., the structure is stable. An HRTEM image of the near-tip region (Figure 2d) shows in more detail a commonly observed arrangement of a 9R polytype band in the middle of the nanowire, bounded by side bands with less ordered stacking faults, which are in turn bounded by side bands of defect free 3C silicon. The two 3C

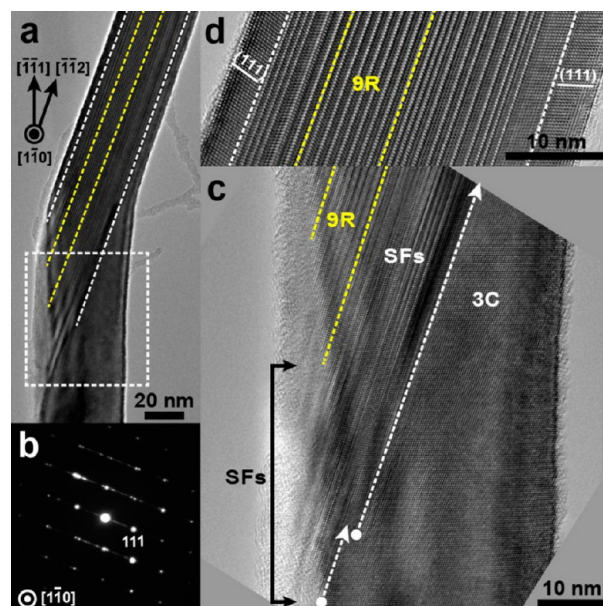


Figure 2. (a) Low-magnification HRTEM image showing a growth direction change from $[111]$ to $[112]$ and the presence of disordered SFs and a polytype band parallel to $[112]$. (b) Diffraction pattern of the nanowire with forbidden reflections along (111) reflections on the $[110]$ zone axis. (c) High-magnification HRTEM image of a boxed area in (b). White dashed arrows represent SFs formed at an early stage of SF band generation. (d) HRTEM image of the nanowire near tip showing the bands of different structures including 3C polytype, disordered SFs, and 9R polytype. White and yellow dashed lines in (a) and (d) are boundaries of 3C/SFs regions and SFs/9R regions, respectively.

side bands have a twin relationship, and the twin boundary is located near the outer surface of the nanowire. This example indicates that the twin boundary is not necessary to initiate formation of the polytype band. However, a single twin defect will generate a bicrystalline nanowire, and the influence of the twin defect on nucleation at the liquid solid interface can provide insight into the stabilization of polytype bands as we describe below.

The bicrystalline nanowire in Figure 3a can be divided into four distinct regions: I, II, III, and IV. Region II is in a twin relation with regions I and IV. Region III exhibits 3-fold periodic contrast variations along $[111]$ that are similar to those seen in images of the 9R polytype. The diffraction pattern (Figure 3b) exhibits $1/3^*(111)$ reflections arising from single and double diffraction from the two twinned crystals. The 9R polytype also exhibits $1/3^*(111)$ reflections, but the relative intensities of the reflections are different from those in two overlapped 3C crystals.^{9,11} In addition, only a single peak at $\sim 300\text{ cm}^{-1}$ is present in the Raman spectrum (inset of Figure 3a), so the nanowire does not contain a polytype. It is well established that overlapping 3C bicrystals can exhibit 9R-like

Table 1. Notations for Various Polytypes with Varying Degrees of Hexagonality

Ramsdell notation	ABC sequence	Hägg notation	Zhdanov notation	h–k notation (hexagonality)
3C	ABC	+++	∞	$(k)_3 (0)$
5H	ABCAC	+++–+	311	kkkhh (0.4)
9R	ABABCBCAC	$(+–)_3$	$(111)_3$	$(kh)_3 (0.67)$
12R	ABCBCABABCAC	$(+–+)_3$	$(211)_3$	$(kkh)_3 (0.5)$
2H	AB	+–	11	$(h)_2 (1)$

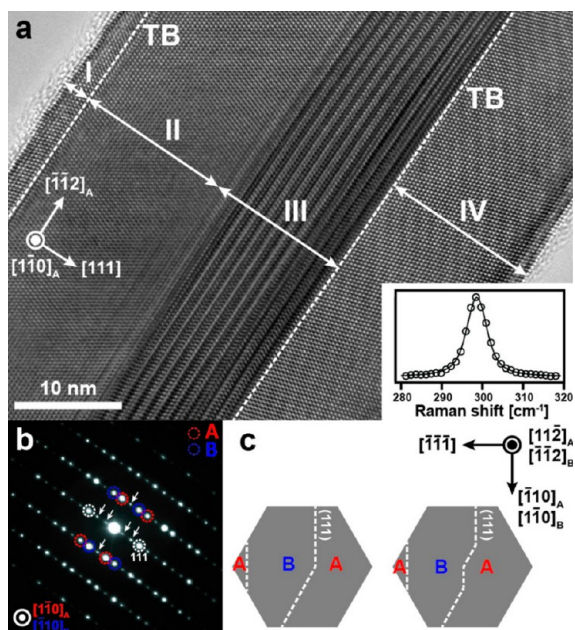


Figure 3. (a) HRTEM image of a nanowire with twinned 3C crystals overlapping along a $\langle 110 \rangle$ zone axis. Dashed lines represent (111) TBs. The zone axis and growth direction are given based on the crystal in regions I and IV that corresponds to crystal A in (c). Inset: Raman spectrum of the nanowire. (b) Diffraction pattern of the nanowire on $\langle 110 \rangle$ zone axes with dotted circles representing reflections from the two crystals, A and B in (c). The white arrows indicate $1/3^*(111)$ reflections arising from double diffraction. (c) Possible cross-sectional structures of the nanowire viewed along the growth direction.

contrast in HRTEM images:^{9,15,29} overlap along the two different $\langle 110 \rangle$ zone axes in a $\langle 110 \rangle$ -oriented nanowire produces “9R-like” contrast when the nanowire axis is not perpendicular to the electron beam,¹⁵ and a $\langle 112 \rangle$ -oriented bicrystalline or polycrystalline nanowire displays similar contrast when $\langle 110 \rangle$ and $\langle 114 \rangle$ orientations of overlapped crystals are parallel to the electron beam.⁹ Figure 3c shows example cross-sectional structures that are consistent with the HRTEM images. Two twinned 3C crystals, A and B, are overlapped along the beam directions, $[1\bar{1}0]_A$ and $[1\bar{1}0]_B$, respectively, and the electron beam diffracted by the two crystals generates the 9R-like contrast of a 3-fold periodicity along $[111]$. The boundary between regions III and IV exhibits a sharp contrast change, indicating the presence of a vertical (111) TB parallel to the electron beam. On the other hand, the Moiré fringes fade away moving from region III to region II, indicating the presence of a boundary inclined to the electron beam. It is possible that the interface is stepped, consisting of alternating vertical (111) TB planes (Figure 3c, right panel). Similar boundaries have been conclusively determined by cross-sectional imaging of Si nanowires with planar defects,⁹ but the precise structure for this particular case is beyond the focus of the present work on polytype generation.

Figure 4a shows that the twinned nanowire shares key characteristics with the polytype nanowires. First, the fault originates at the “outer” surface (Figure 4b for twinned nanowires and Figure 2a for polytype nanowires), as also seen in bicrystalline Si nanowires.²² Second, the TB and the generated polytype segments precede a kink from a $[1\bar{1}1]$ to a $[1\bar{1}2]$ growth direction. Third, the (111) TB propagates along $[1\bar{1}2]$ as observed for the (111) SFs in polytype nanowires.

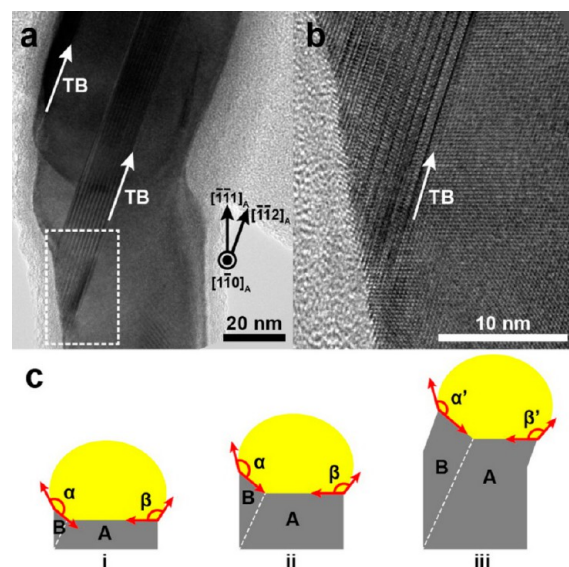


Figure 4. (a) HRTEM image of the nanowire in Figure 3 showing a growth direction change from $[1\bar{1}1]$ to $[1\bar{1}2]$ for crystal A. White arrows indicate two TBs on (111) planes. (b) HRTEM image of the region in the dashed white box area in (a). (c) Simplified schematic of the bicrystalline nanowire cross section showing steps of nanowire kinking. α and β represent wetting angles at different positions of the TPB. α' and β' are wetting angles after the nanowire kinks. White dashed lines are (111) TB between two crystals, A and B.

The similarities between the generation location and the propagation direction of the SF and TB indicate that they share a similar origin in faulted nucleation within the $\langle 111 \rangle$ -oriented segment. In situ microscopy and modeling have shown that nucleation occurs on small truncation facets that connect the $\{111\}$ growth facet to the triple-phase boundary.^{22,30,31} When the small facet is a (111) plane, a single nucleation event with a faulted stacking sequence generates a (111) SF, and the two consecutive faulted nucleations generate a (111) TB.²² It has been proposed previously that increasing the supersaturation of the catalyst reduces the difference in the barriers to nucleation of faulted versus unfaulted planes, leading to increased stacking fault generation and kinking.²⁰ This model is consistent with our observations. While polytype nanowires include multiple SFs, twinned bicrystalline nanowires have only one (or at most two) twin boundaries. On the basis of the observations above, we hypothesize that in polytype nanowires a corner facet acts as a site of persistent nucleation, whereas in the twinned nanowires, the twin boundary pins nucleation site as suggested previously.^{22,32} A recent study on new phase nucleation in a twinned Si nanowire has shown with conclusive in situ TEM observations that such nucleation is pinned at the TB³³ and supports our hypothesis.

Figure 4c illustrates how growth fronts evolve in the twinned bicrystalline nanowires. Together with the TB formation, a new twinned growth front, 140° apart from the preexistent growth front, emerges. This new facet reduces the influence of the prior corner facet on nucleation of successive (111) planes. As the TB propagates along $[1\bar{1}2]$ in the $[1\bar{1}1]$ -oriented segment, the new growth facet expands while the pre-existing growth facet shrinks. Consequently, the distance between the two TPB points at the opposite sides increases and the wetting angle of the droplet near the inclined facet (α) decreases. The TPB is fixed at the edges connecting the growth facets and the side

walls, but there is a finite range of the wetting angle for which the droplet is stable against unpinning.³⁴ Once the wetting angle, α , reaches the unpinning limit, further expansion and shrinkage of growth facets no longer occur. Instead, the nanowire kinks to the $[\bar{1}\bar{1}2]$ direction, a stable wetting angle is restored, and both growth facets advance. In fact, the role of TB and twinned growth facet in inducing the nanowire kinking was previously proposed for Si nanowires.²² Continuum modeling has also shown how nanowire kinking arises from changes in droplet volume and wetting angle that lead to unpinning.^{34,35}

Figure 5 illustrates a layer-by-layer growth model of polytype nanowires informed by the previously described model of

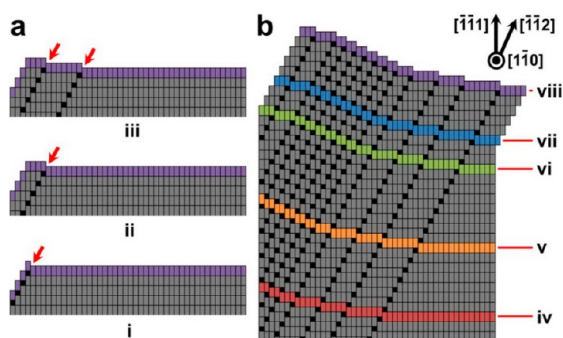


Figure 5. A proposed model of layer-by-layer growth for the polytype nanowire. A series of black squares represent a SF: (a) Generation of atomic steps at L–S interface due to faulted nucleation and SF formation. The red arrows point out the atomic steps. (b) Evolution of an inclined pseudofacet due to accumulated atomic steps on L–S interface and nanowire kinking. The growth fronts at different times (stages of iv, v, vi, vii, and viii) are color-coded.

twinned bicrystalline nanowires in which stacking faults pin nucleation. First, a single (111) SF is generated as a result of the faulted nucleation on a corner facet (step i in Figure 5a). The (111) SF produces an atomic step on the main $(\bar{1}\bar{1}1)$ facet, and this becomes the preferred nucleation site. The (111) SF then propagates toward $[\bar{1}\bar{1}2]$ without generating additional planar defects (step ii). After the growth of a few layers, faulted nucleation on the corner facet occurs once again, seeding another SF parallel to the preexisting one and producing another atomic step at the L–S interface (step iii). Multiple faulted nucleations on the corner facet are possible because of the high supersaturation in the growth seed. As a result, a number of SFs with an irregular spacing are formed together with new atomic steps on the L–S interface. In most of the nanowires examined, the density of SFs increases to a point where periodic nucleation becomes favored, leading to a polytype band. As the atomic steps build up on the outside of the nanowire due to the faulted nucleations on the same corner facet, this portion of the L–S interface defines a growth front that is inclined to the original $(\bar{1}\bar{1}1)$ facet. Figure 5b illustrates how the inclined pseudofacet evolves with the nucleation of multiple stacking faults during nanowire growth. The pseudofacet serves a similar role to the twinned facet in the bicrystalline nanowires as the distance between the two opposite-side TPB points increases and the droplet morphology evolves. We noted above that the length of the nanowire between the location of first planar defect initiation and kinking is larger in polytype nanowires than in twinned nanowires. This is consistent with the fact that in polytype nanowires many atomic steps are required to form the inclined growth front,

whereas in twinned nanowires, a single TB readily generates a 140° -inclined growth facet. Once the wetting angle on the slanted pseudofacet reaches the critical condition for sustaining a stable growth seed, the nanowire kinks in a similar fashion to that described in Figure 4c.

We now consider more closely how periodicity might arise in the SFs. For example, in order to complete one unit cell of 9R polytype with ABABCBCAC stacking sequence, faulted nucleation needs to occur for every third Ge bilayer, three times in a row. Such an orderly process seems unlikely considering the random nature of nucleation and the number of available sites. We hypothesize that if the generated SFs happen to initiate short-range order, that is, the atomic steps are regularly spaced over a few planes, the corresponding portion of L–S interface may begin to act as a flat facet of moderate index. This polytype pseudofacet will be specific to the stacking sequence of polytype, but one could expect a pseudo- $(\bar{1}\bar{1}2)$ facet to form perpendicular to the growth direction in Figure 5b. Intriguingly, the portion of L–S interface corresponding to polytype band appears to exhibit a sharp facet in ex situ images (see Supporting Information Figure 1). By analogy to the growth of the twinned bicrystalline nanowire, it is possible that nucleation then preferentially occurs in the atomically rough region between the main facet and the polytype facet. Compared to the case of the twinned nanowire, the existence of the polytype facet does not as strongly reduce the probability of faulted nucleation on the outside (111) corner facet, as we do observe SFs at the outer side of polytype band.

The above hypothesis is based in part on ex situ TEM images of the catalyst–nanowire interface, so we must emphasize that the morphology of L–S interface, which is hard to observe in situ with atomic resolution during growth, may not be precise. Nonetheless, the evolution of the polytype facet proposed here is strongly suggested from the observed evolution of the nanowire morphology and from numerous other relevant in situ and ex situ observations of L–S interface composed of two or more facets or a high-index facet in different material systems. The recent in situ TEM observation of NiSi_2 nucleation pinning at the TB interface in a twinned Si nanowire further substantiates our hypothesis.³³ Furthermore, the postulation of a sharp facet at the growth seed/nanowire interface in the polytype band region is consistent with other observations of multiply faceted L–S interfaces composed of low-index Si facets^{32,36} and high-index InAs and ZnO facets in non- $\langle 111 \rangle$ oriented nanowires.^{37,38}

In summary, we propose that polytypes in Ge nanowires can be generated through multiplication of SFs on the corner facet followed by evolution of a growth pseudofacet associated with ordered SFs. Stacking sequences of 5H, 9R, and 12R polytypes in Ge nanowires were clearly identified via C_s -corrected HAADF STEM. We also confirmed that Raman spectroscopy can reliably discriminate between polytype and bicrystalline Ge nanowires, as shown previously for Si nanowires.^{9,11} We related the layer-by-layer growth mechanism of bicrystalline nanowires to that of polytype nanowires by considering the evolution of the nucleation site, the growth front, and the droplet morphology. From this comparison, we proposed that the nature of the initiating planar defect (TB or SF) determines the final structure of nanowire (twinned or polytype). Given the similarities in the generation mechanisms between the two structures, synthesis conditions that influence the types of planar defect to be seeded should be explored to bias the growth of polytype or bicrystalline nanowires. While exper-

imentally challenging, in situ TEM studies and cross-sectional imaging are compelling future directions to validate this model and approach.^{9,39–41} Alternatively, template-assisted growth is another promising approach to grow polytype nanowires in a more controlled manner while potentially avoiding changes in growth direction.¹³

■ ASSOCIATED CONTENT

■ Supporting Information

HRTEM images of multiply faceted Au–Ge interfaces. This material is available free of charge via the Internet at <http://pubs.acs.org>.

■ AUTHOR INFORMATION

■ Corresponding Author

*E-mail lahon@northwestern.edu (L.J.L.).

■ Notes

The authors declare no competing financial interest.

■ ACKNOWLEDGMENTS

This work was supported by NSF under DMR-1006069. Nanowire growth and Raman spectroscopy were performed at Northwestern University. Microscopy in this work was performed, in part, at the EPIC facility of NUANCE Center. The NUANCE Center is supported by NSF-NSEC, NSF-MRSEC, Keck Foundation, the State of Illinois, and Northwestern University. We thank Dr. Masahiro Kawasaki from JEOL USA, Inc., and Akira Yasuhara from JEOL Ltd., Japan, for their help with C_v-corrected TEM imaging. S.A.D. acknowledges support from a faculty start-up grant at UC San Diego.

■ REFERENCES

- (1) Algra, R. E.; Verheijen, M. A.; Borgstrom, M. T.; Feiner, L.-F.; Immink, G.; van Enckevort, W. J. P.; Vlieg, E.; Bakkers, E. P. A. M. *Nature* **2008**, *456*, 369–372.
- (2) Caroff, P.; Dick, K. A.; Johansson, J.; Messing, M. E.; Deppert, K.; Samuelson, L. *Nat. Nanotechnol.* **2009**, *4*, 50–55.
- (3) Dick, K. A.; Thelander, C.; Samuelson, L.; Caroff, P. *Nano Lett.* **2010**, *10*, 3494–3499.
- (4) Murayama, M.; Nakayama, T. *J. Phys. Soc. Jpn.* **1992**, *61*, 2419–2433.
- (5) Murayama, M.; Nakayama, T. *Phys. Rev. B* **1994**, *49*, 4719–4724.
- (6) Persson, C.; Janzén, E. *J. Phys.: Condens. Matter* **1998**, *10*, 10549.
- (7) Gu, L.; Yu, Y.; Sigle, W.; Usami, N.; Tsukimoto, S.; Maier, J.; Ikuhara, Y.; van Aken, P. A. *Appl. Phys. Lett.* **2010**, *97*, 213102.
- (8) Dayeh, S. A.; Liu, X. H.; Dai, X.; Huang, J. Y.; Picraux, S. T.; Soci, C. *Appl. Phys. Lett.* **2012**, *101*, 053121.
- (9) Hemesath, E. R.; Schreiber, D. K.; Kisielowski, C. F.; Petford-Long, A. K.; Lauhon, L. J. *Small* **2012**, *8*, 1717–1724.
- (10) Lopez, F. J.; Givan, U.; Connell, J. G.; Lauhon, L. J. *ACS Nano* **2011**, *5*, 8958–8966.
- (11) Lopez, F. J.; Hemesath, E. R.; Lauhon, L. J. *Nano Lett.* **2009**, *9*, 2774–2779.
- (12) Davidson, F. M.; Lee, D. C.; Fanfair, D. D.; Korgel, B. A. *J. Phys. Chem. C* **2007**, *111*, 2929–2935.
- (13) Barth, S.; Boland, J. J.; Holmes, J. D. *Nano Lett.* **2011**, *11*, 1550–1555.
- (14) Shin, N.; Chi, M.; Howe, J. Y.; Filler, M. A. *Nano Lett.* **2013**, *13*, 1928–1933.
- (15) Hertog, M. I. d.; Cayron, C.; Gentile, P.; Dhalluin, F.; Oehler, F.; Baron, T.; Rouviere, J. L. *Nanotechnology* **2012**, *23*, 025701.
- (16) Carim, A. H.; Lew, K. K.; Redwing, J. M. *Adv. Mater.* **2001**, *13*, 1489–1491.
- (17) Madras, P.; Dailey, E.; Drucker, J. *Nano Lett.* **2009**, *9*, 3826–3830.

- (18) Hyun, Y.-J.; Lugstein, A.; Steinmair, M.; Bertagnolli, E.; Pongratz, P. *Nanotechnology* **2009**, *20*, 125606.
- (19) Tian, B.; Xie, P.; Kempa, T. J.; Bell, D. C.; Lieber, C. M. *Nat. Nanotechnol.* **2009**, *4*, 824–829.
- (20) Glas, F.; Harmand, J.-C.; Patriarche, G. *Phys. Rev. Lett.* **2007**, *99*, 146101.
- (21) Su, Z.; Dickinson, C.; Wan, Y.; Wang, Z.; Wang, Y.; Sha, J.; Zhou, W. *CrystEngComm* **2010**, *12*, 2793–2798.
- (22) Dayeh, S. A.; Wang, J.; Li, N.; Huang, J. Y.; Gin, A. V.; Picraux, S. T. *Nano Lett.* **2011**, *11*, 4200–4206.
- (23) Hägg, G. *Ark. Kemi, Mineral. Geol.* **1943**, *16B*, 3.
- (24) Verma, A. R.; Krishna, P. *Polymorphism and Polytypism in Crystals*; Wiley: New York, 1966; pp 83–91.
- (25) Zhdanov, G. S. *C. R. Acad. Sci. U.R.S.S.* **1945**, *48*, 43.
- (26) Nakashima, S.; Katahama, H.; Nakakura, Y.; Mitsuishi, A. *Phys. Rev. B* **1986**, *33*, 5721–5729.
- (27) Nakashima, S.; Ohta, H.; Hangyo, M.; Palosz, B. *Philos. Mag. B* **1994**, *70*, 971–985.
- (28) Rohmfeld, S.; Hundhausen, M.; Ley, L. *Phys. Rev. B* **1998**, *58*, 9858–9862.
- (29) Cayron, C.; Den Hertog, M.; Latu-Romain, L.; Mouchet, C.; Secouard, C.; Rouviere, J.-L.; Rouviere, E.; Simonato, J.-P. *J. Appl. Crystallogr.* **2009**, *42*, 242–252.
- (30) Gamalski, A. D.; Ducati, C.; Hofmann, S. J. *Phys. Chem. C* **2011**, *115*, 4413–4417.
- (31) Wen, C. Y.; Tersoff, J.; Hillerich, K.; Reuter, M. C.; Park, J. H.; Kodambaka, S.; Stach, E. A.; Ross, F. M. *Phys. Rev. Lett.* **2011**, *107*, 025503.
- (32) Hemesath, E. R.; Schreiber, D. K.; Gulsoy, E. B.; Kisielowski, C. F.; Petford-Long, A. K.; Voorhees, P. W.; Lauhon, L. J. *Nano Lett.* **2012**, *12*, 167–171.
- (33) Tang, W.; Picraux, S. T.; Gusak, A. M.; Huang, J. Y.; Tu, K. N.; Dayeh, S. A. *Nano Lett.* **2013**, *13*, 2748–2753.
- (34) Schwarz, K. W.; Tersoff, J. *Nano Lett.* **2011**, *11*, 316–320.
- (35) Schwarz, K. W.; Tersoff, J. *Phys. Rev. Lett.* **2009**, *102*, 206101.
- (36) Wu, Y.; Cui, Y.; Huynh, L.; Barrelet, C. J.; Bell, D. C.; Lieber, C. M. *Nano Lett.* **2004**, *4*, 433–436.
- (37) Xu, H.; Wang, Y.; Guo, Y.; Liao, Z.; Gao, Q.; Tan, H. H.; Jagadish, C.; Zou, J. *Nano Lett.* **2012**, *12*, 5744–5749.
- (38) Ding, Y.; Gao, P. X.; Wang, Z. L. *J. Am. Chem. Soc.* **2004**, *126*, 2066–2072.
- (39) Hillerich, K.; Dick, K. A.; Wen, C.-Y.; Reuter, M. C.; Kodambaka, S.; Ross, F. M. *Nano Lett.* **2013**, *13*, 903–908.
- (40) Wen, C. Y.; Tersoff, J.; Reuter, M. C.; Stach, E. A.; Ross, F. M. *Phys. Rev. Lett.* **2010**, *105*, 195502.
- (41) Kim, B. J.; Tersoff, J.; Kodambaka, S.; Reuter, M. C.; Stach, E. A.; Ross, F. M. *Science* **2008**, *322*, 1070–1073.